FLUX-ROPE CORONAL MASS EJECTION GEOMETRY AND ITS RELATION TO OBSERVED MORPHOLOGY

J. KRALL

Plasma Physics Division, Naval Research Laboratory, Washington, DC 20375-5000

AND

O. C. ST. CYR

Solar Physics Branch, NASA-Goddard Space Flight Center, Greenbelt, MD 20771; and Department of Physics,
The Catholic University of America, Washington, DC 20064

ABSTRACT

A simple parameterization of a three-dimensional flux rope is used to determine a "typical flux-rope geometry" that corresponds to observed flux-rope coronal mass ejection (CME) morphologies (average apparent angular widths) at a leading-edge height of about 5.5 $R_\odot$. The parameterized flux rope, the curved axis of which is assumed to trace out an ellipse, is described in terms of the eccentricity of the ellipse, the width (minor diameter d) of the flux rope at the apex, and the height of the apex above the solar surface $2R_1$. Assuming self-similar expansion, there are only two geometrical parameters to be determined: the eccentricity ϵ and the axial aspect ratio $\Lambda_a \equiv 2R_1/d$. For each pair of geometrical parameters, an ensemble of 72 orientations is considered, with each being specified in terms of a latitude angle, a longitude angle, and a rotation about the direction of motion. The resulting ensemble of synthetic coronagraph images is used to produce statistical measures of the morphology for comparison to corresponding observational measures from St. Cyr et al. (2004). We find that a typical flux-rope CME has $\epsilon = 0.7 \pm 0.2$ and $\Lambda_a = 1.1 \pm 0.3$.

Subject headings: Sun: coronal mass ejections (CMEs)

1. INTRODUCTION

The shape of a coronal mass ejection (CME) as seen in a coronagraph image depends on the underlying magnetic geometry, the population of that geometry by solar or heliospheric plasma, Thomson scattering from the free electrons, and the observed projection of the resulting light onto the two-dimensional (2D) plane of the sky. In this way, three-dimensional (3D) CME geometries are reduced to 2D CME morphologies. These morphologies have been the subject of numerous measurements (see, e.g., Howard et al. 1985; Illing & Hundhausen 1986) and descriptions (e.g., the "three part structure" of Hundhausen 1999), leading, in turn, to considerable speculation about the nature of the corresponding geometry. Such speculations include the first identification of halo CMEs as Earth-directed structures (Howard et al. 1982) and the "ice cream cone" model (Fisher & Munro 1984).

In recent years, a great deal of this speculation has centered on events that are described as having morphologies consistent with an underlying flux-rope geometry (Chen et al. 1997; Dere et al. 1999; Wood et al. 1999; Wu et al. 1999; Chen et al. 2000; Plunkett et al. 2000; Krall et al. 2001; Chen & Krall 2003). Krall et al. (2001) measured and modeled 11 such events, identifying them as "flux-rope CMEs."

Recently, St. Cyr et al. (2004) identified 27 near-limb CME events that appeared to be flux-rope CMEs, oriented to give either an "axial" view (Fig. 1a) or a "broadside" view (Fig. 1b) of the underlying flux-rope geometry. In that study, flux-rope morphologies were limited to CMEs with both a three-part structure and a well-defined leading-edge feature that encompasses the CME and appears to remain connected to the Sun. Axial events were further limited to those with a concave-outward tailing-edge feature, the appearance of multiple concentric curved features between the leading and trailing edges, and a source-region neutral line roughly parallel to the plane of the ecliptic. Broadside events were further limited to those with an overarching looplike struc-

ture and a source-region neutral line roughly perpendicular to the plane of the ecliptic (Cremades & Bothmer 2004). In all cases, a solar source region was identified and was located within 30° from the limb. For all events, the CMEs themselves, measured at leading-edge heights ranging from 4.5 to 6.5 $R_\odot$, had central position angles within 50° of the equator. For the axial events, the average apparent angular width was 48° ± 12°; for the broadside events, the average width was 78° ± 17° (St. Cyr et al. 2004).

Note that the selection of events in St. Cyr et al. (2004) excluded high-latitude polar-crown events, which often feature very long neutral lines and are therefore expected to have wider footpoint separations than other flux-rope CME populations. For example, Chen & Krall (2003) showed that the wide footpoint separation and underlying flux-rope geometry that was hypothesized for the 1998 June 2 polar-crown eruption is confirmed by its atypical acceleration profile.

In this paper we present a two-variable parameterization of a flux-rope CME geometry. By considering an appropriate range of geometrical parameters and orientation angles, and by computing the corresponding morphology via a Thomson-scattering calculation for each of the many resulting cases, we find that we can determine a unique CME geometry that reproduces the average apparent angular widths that were reported in the morphological study of St. Cyr et al. (2004).

In the following sections we describe, in turn, the CME parameterization, the procedure by which statistical results are obtained, the results themselves, and a brief discussion. Here the intent is to determine geometrical parameters that best fit the observations and therefore to provide a quantitative geometrical description of a typical flux-rope CME.

2. FLUX-ROPE CME PARAMETERIZATION

We describe a flux rope as having a curved axis and, at each point along the axis, a circular cross-section. In keeping with
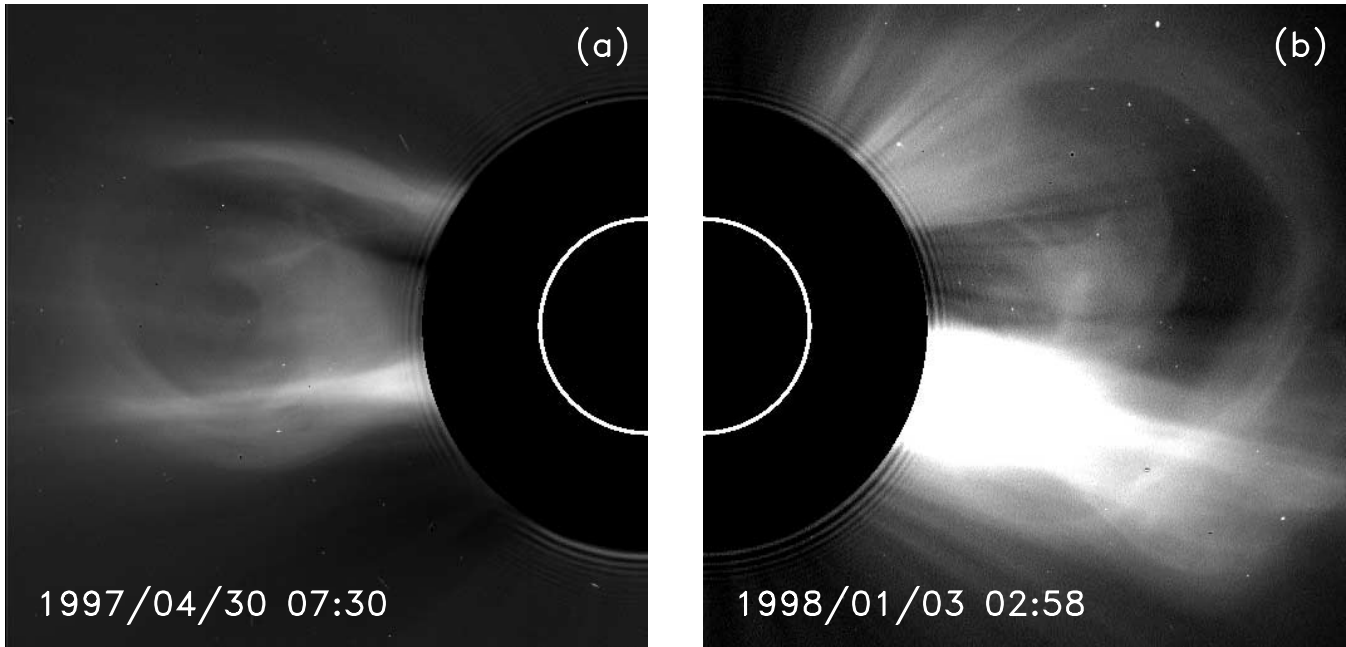
Fig. 1.—LASCO/C2 coronagraph images from (*a*) 1997 April 30 showing an "axial" morphology and (*b*) 1998 January 3 showing a "broadside" morphology. Note that the bright streamer in the lower part of image (*b*) is not part of the eruption.

the observations, the width (minor diameter) is narrowest at the footpoints on the solar surface and thickest at the apex, where the width is d. Generally in keeping with the observations, but also to simplify the parameterization, we assume that the curved axis of the flux rope traces out an ellipse. This is illustrated in Figure 2, which shows synthetic coronagraph images of exactly axial (Fig. 1*a*) and exactly broadside (Fig. 1*b*) views of our specified flux-rope geometry, corresponding to two views of a flux-rope CME whose apex is moving radially outward from the west limb. In Figure 2*b*, it is clear that the axis of the flux rope traces out an ellipse, which we refer to as the flux-rope ellipse.

We parameterize the flux rope in terms of the eccentricity ϵ of the flux-rope ellipse and the "axial aspect ratio" Λ_a, which is the ratio of major diameter of the flux-rope ellipse to the apex diameter. For example, consider a flux rope where the flux-rope ellipse has a major axis of length $2R_1$, a minor axis length $2R_2$, and an apex width d, as indicated in Figure 2. Here the eccentricity is $\epsilon = [1 - (R_2/R_1)^2]^{1/2}$ and the axial aspect ratio is $\Lambda_a = 2R_1/d$. Note that at a leading-edge height of 5.5 $R_\odot$ the resulting morphology is only a weak function of the footpoint separation, which is therefore not accounted for. Note also that the axial aspect ratio defined here differs in several respects from the superficially similar aspect ratio reported in Chen et al. (1997) and Krall et al. (2001), which is the ratio of apex height to apex width in a CME image and has been applied only to events displaying axial morphology. In other words, the Chen-Krall aspect ratio corresponds to an image of a flux-rope CME projected onto the plane of the sky rather than to the underlying structure.

If we had a way of knowing (as of this writing, we do not) that a flux-rope CME was at the limb with its apex moving exactly radially outward, and was oriented so that it was viewed exactly axially, then Λ_a could be easily measured from a CME image as in Figure 2*a*. Similarly, if a flux-rope CME was at the limb with its apex moving exactly radially outward, and was oriented so that it was viewed exactly broadside, as in Figure 2*b*, then the ellipse eccentricity could be easily measured from a CME image.
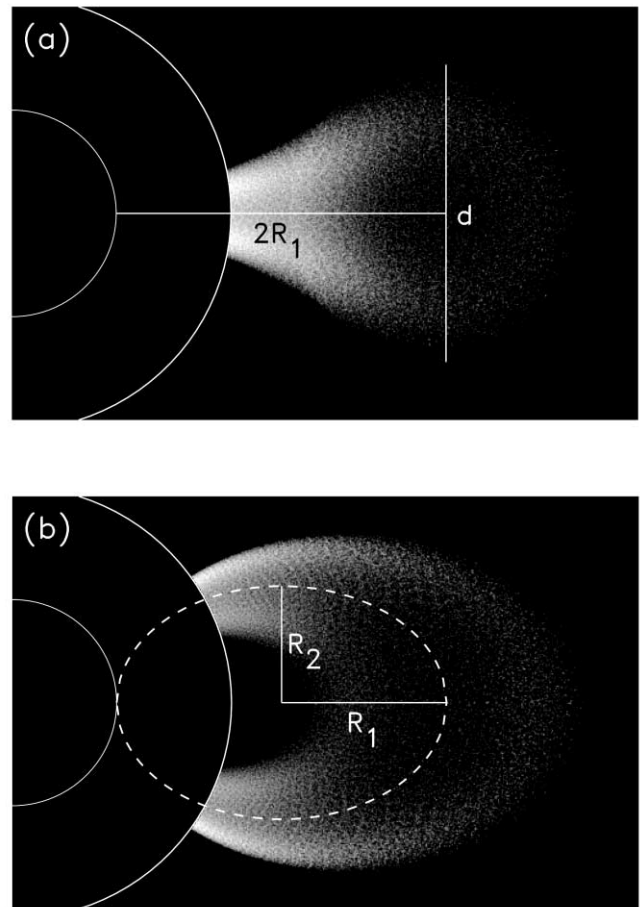

Fig. 2.—Synthetic coronagraph images of a parameterized flux rope showing (*a*) axial and (*b*) broadside views. Here, $\epsilon = 0.70$ and $\Lambda_a = 1.1$.

Instead we must infer the typical underlying geometry from 2D images taken of multiple events.

3. PROCEDURE

We use synthetic coronagraph images to make the connection between the underlying geometry and the observed morphology (see Appendix A for details on the generation of synthetic coronagraph images of a parameterized flux rope). In particular, we are interested in determining a pair of geometrical parameters that can reproduce the statistical measures of flux-rope CME morphology that were obtained in the observational study of St. Cyr et al. (2004). In other words, we wish to obtain a statistical result that is in agreement with the observed statistical result.

Our statistical result is obtained by measuring a set of synthetic coronagraph images that are generated from a given pair of flux-rope parameters, ϵ and Λ_a. For a single pair of parameters, we consider an array of possible orientation angles (two source location angles and one tilt angle) consistent with the observational study of St. Cyr et al. (2004). From the resulting set of synthetic coronagraph images we determine (1) the average apparent angular extent of the cases that appear to be "axial" views, and (2) the average apparent angular extent of the cases that appear to be "broadside" views. Consistent with the measurements of St. Cyr et al. (2004), all synthetic coronagraph images are computed so as to be comparable to LASCO/C2 images (Brueckner et al. 1995), with an "occulting disk" of radius 2.1 $R_\odot$. Also consistent with the St. Cyr et al. (2004) study, the projected (morphological) position of the CME leading edge is at the same specified height, 5.5 $R_\odot$, in all cases.

For a given pair of flux-rope geometrical parameters, the orientation angles to be varied are the tilt of the flux rope about the axis defined by the direction of motion (α_y), the source latitude (λ_0), and the source longitude (ϕ_0). For the purpose of orienting the flux rope, we define a coordinate system with its origin at Sun center, the z-axis upward, the x-axis directed toward the west limb, and the y-axis directed along the Earth-Sun line, away from Earth.

When orienting the flux rope, we begin with the flux-rope ellipse in the plane of the ecliptic, situated so that one end of the major axis of the ellipse (the "footpoints") sits on the solar surface at disk center. The flux rope extends outward from that point, as would be the case for a front-side halo CME. We apply the tilt angle α_y (a rotation about y), then move the source location to the correct latitude λ_0 (a rotation about x), and finally move the source to the correct longitude (a rotation about z). Thus $\alpha_y = 0$, $\lambda_0 = 0$, and $\phi_0 = 90°$ correspond to a west-limb event at the solar equator, viewed exactly axially, as in Figure 2a, and $\alpha_y = \pm 90°$, $\lambda_0 = 0$, and $\phi_0 = 90°$ correspond to Figure 2b. Another example of the application of these orientation angles to a specified flux rope can be found in Figure 8 of Krall et al. (2006).

For simplicity, the angular distribution of flux ropes will be assumed to be uniform within our chosen range of angles: $90° \leq \alpha_y < -90°$, $0° \leq \lambda_0 \leq 50°$, and $-50° \leq \phi_0 \leq -90°$. This range of angles was chosen for consistency with the St. Cyr et al. (2004) study. Specifically, our specified latitudes correspond to the range of position angles for the chosen events; the latitudes used in this study are $\lambda_0 = 8°$, $25°$, and $42°$. In the study of St. Cyr et al. (2004) a source location was determined for each event, with all source longitudes lying within $30°$ of the limb. However, each of these observed events could be deflected in longitude, to an unknown degree. Based on Webb et al. (2000), Krall et al. (2006), and Yurchyshyn et al. (2006) we conclude that $10°$ deflections are common and so allow longitudes up to $40°$ from the limb; the

longitudes used in this study are $\phi_0 = -57°$, $-70°$, and $-83°$. To avoid redundant images, latitude and longitude angles are limited to the intersection of the northern, eastern, and Earthward solar hemispheres. Because the St. Cyr et al. (2004) study places no clear restriction on the tilt angle (α_y), all possible tilt angles are considered. We use $\alpha_y = -79°$, $-56°$, $-34°$, $-11°$, $11°$, $34°$, $56°$, and $79°$, which are evenly spaced within the range $90° \leq \alpha_y \leq -90°$. For each pair of geometrical parameters (ϵ and Λ_a) we consider the full set of orientation angles given above, resulting in 72 synthetic coronagraph images, each generated with a projected leading-edge height of 5.5 $R_\odot$.

Note that certain assumptions about flux-rope CME dynamics are implied above. Specifically, by considering fixed values for ϵ and Λ_a over a range of apex heights above the solar surface, we assume self-similar expansion of the flux-rope geometry (our range of apex heights is imposed by the specified variation in orientation angles at a fixed projected leading-edge height). Previous modeling efforts (Chen et al. 1997; Krall et al. 2001, 2006) show that this is a reasonable assumption within the LASCO field of view. In addition, our specification of the orientation angles describes only cases in which the flux-rope apex moves radially outwards from the chosen latitude and longitude. The possibility of nonradial motion is accounted for in that (1) our range of latitudes (λ_0 within $50°$ of the equator) is chosen based on position angles from coronagraph images, rather than source locations, and (2) our range of longitudes (ϕ_0 within $40°$ of the limb) is based on the range of source locations (within $30°$ of the limb) plus $10°$ to account for possible deflections. We might instead have specified a range of deflection angles (α_x, α_z) in addition to a range of source locations. However, given the imprecise observational numbers to which we are comparing our results (axial extent $48° \pm 12°$, broadside extent $78° \pm 17°$), the introduction of deflection angles was deemed redundant.

For a given pair of geometrical parameters (ϵ and Λ_a) each of the resulting set of 72 images is examined to determine if it appears to be either an axial or a broadside view of a flux rope. Here the key criteria are the presence of a concave-outward feature as a component of a circular apex feature (for axial cases) or an overarching loop structure with an inner cavity and inner loop (for broadside cases). Those that are not clearly in either classification are deemed "complex" (Howard et al. 1985) and are not considered further. For a given pair of geometrical parameters, angular extents for the axial and broadside cases are recorded and the corresponding average angular extents are computed. For example, Figure 3 illustrates three orientations of a flux rope with fixed values $\epsilon = 0.7$, $\Lambda_a = 1.1$, $\lambda_0 = 8°$, and $\phi_0 = -70°$. Figure 3a has $\alpha_y = 11°$ and an axial morphology, Figure 3b has $\alpha_y = 56°$ and a broadside morphology, and Figure 3c has $\alpha_y = 34°$, resulting in a complex morphology. Here the relevant angular extents are $45°$ (Fig. 3a) and $72°$ (Fig. 3b).

Comparing Figures 1 and 3, we note projection effects, particularly in the axial images. In Figure 3a, for example, the view is not exactly axial, and while one leg appears as a pair of relatively bright features connecting the round CME apex to the occulting disk, the other leg (presumably farther from the plane of the sky and therefore showing a weaker degree of Thomson scattering) is visible as a fainter feature to the south. The second leg of the flux rope also clearly connects the round CME apex to the occulting disk. In Figure 3c, the flux rope is tilted far enough from the axial view that the concave-outward feature is shifted away from the center of the synthetic CME, and a morphology that is neither clearly axial nor clearly broadside is obtained. In this context, Figure 1a, which has an angular width of $50°$ (St. Cyr et al. 2004),
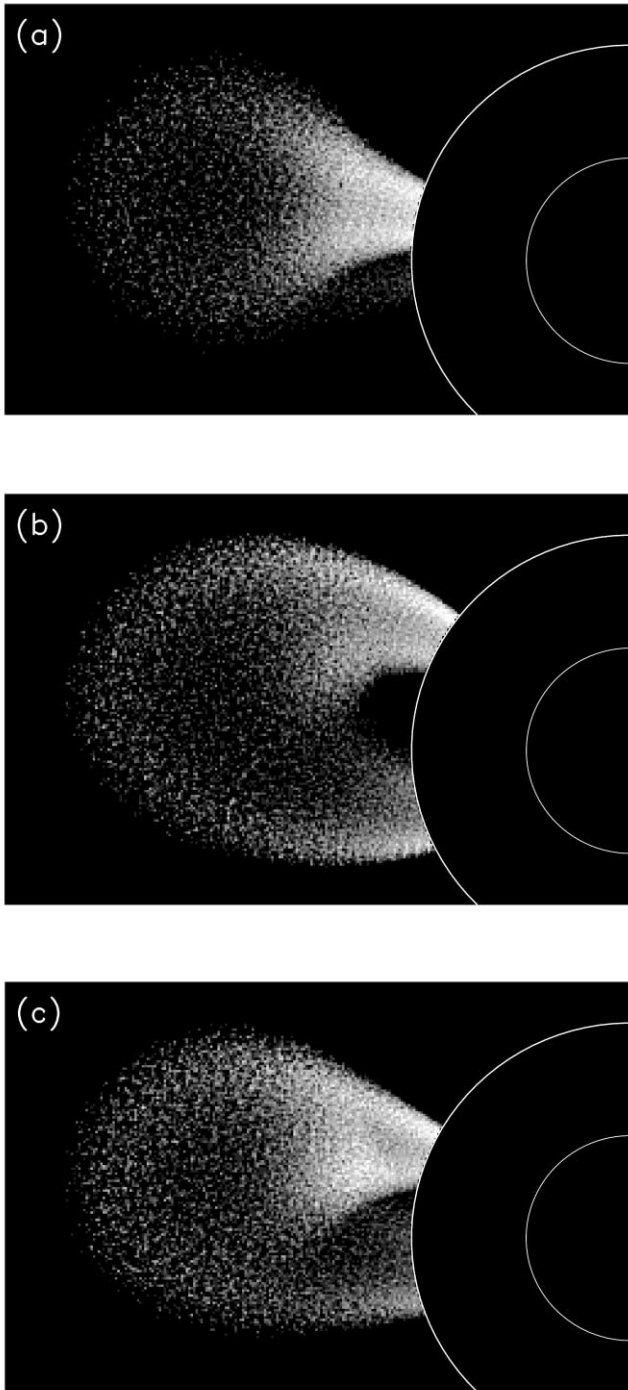
FIG. 3.—Three orientations of a flux rope showing (*a*) axial morphology, (*b*) broadside morphology, and (*c*) complex morphology.

would seem to be to be an example of a flux rope that is shifted slightly away from the axial view so that the concave-outward feature is slightly off center. Lacking the concave-outward feature of the axial morphology, projection effects in broadside images are less clear. We do note, however, that the inner void in Figure 3*b*, which lies between the legs of the flux rope, appears to have a counterpart in Figure 1*b*, suggesting that that event (angular width 80°; St. Cyr et al. 2004) might be close to an exactly broadside orientation. However, this inner void feature in broadside CME images has not been noted as often as the concave-outward feature in axial CMEs; it may not be as universal.
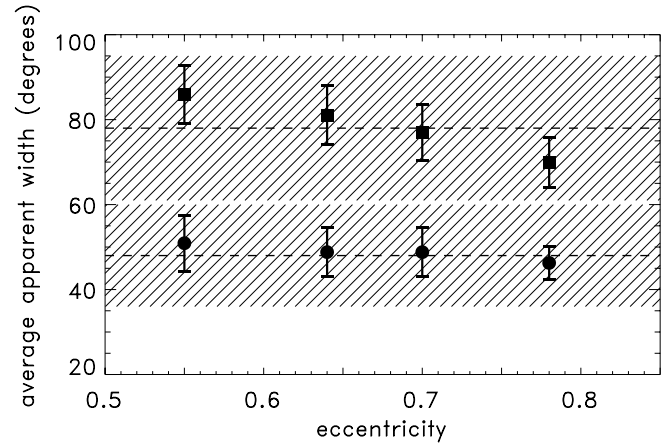

FIG. 4.—Numerically determined average angular widths for the axial (*filled circles*) and broadside (*filled squares*) cases are plotted vs. eccentricity ϵ at a fixed value of the axial aspect ratio $\Lambda_a = 1.1$. Observational results from St. Cyr et al. (2004) for the axial and broadside cases are indicated by horizontal lines at 48° and 78°, respectively. Uncertainties in the observational results are indicated by shaded areas.

The best-fit geometrical specification is obtained by determining, by trial and error, a pair of flux-rope geometrical parameters that reproduces the average apparent widths, from St. Cyr et al. (2004) for both the axial CME events and the broadside CME events. In this best-fit case, we are comparing two ensembles. In the observed ensemble there is a distribution of orientation angles and of geometrical parameters. In the numerically generated ensemble, the distribution of orientation angles is approximately the same as in the observations, and the (unknown) actual distribution of geometries is replaced by a single fixed geometry. We assume that these two ensembles are equivalent in the sense that a sequence of measurements at fixed position is equivalent to an ensemble of possible states at a fixed time for a stationary ergodic ensemble (Reif 1965). The resulting best-fit geometry constitutes a prediction of a "typical CME geometry" that can be tested by future observations with spacecraft such as *Solar Terrestrial Relations Observatory* (*STEREO*).

4. RESULTS

Figure 4 shows statistical results for a parameterized flux rope with fixed axial aspect ratio $\Lambda_a = 1.1$ and various values of the eccentricity, $\epsilon = 0.55, 0.64, 0.70,$ and 0.78. In each case the average axial (*filled circle*) and broadside (*filled square*) widths are shown along with error bars, indicating the standard deviation within the ensemble. For example, for $\Lambda_a = 1.1$ and $\epsilon = 0.70$, 25 of the 72 images showed axial morphologies, and 34 images showed broadside morphologies. As indicated in Figure 4, the average axial width of the axial images was $48°.8 \pm 5°.7$; the average axial width of the broadside images was $77°.0 \pm 6°.5$ in this case.

In Figure 4, the observational results of St. Cyr et al. (2004) are indicated by horizontal lines, with shaded areas indicating the uncertainties. This figure clearly shows that the best agreement between the parameterized flux rope and the observations occurs at $\Lambda_a = 1.1$ and $\epsilon = 0.70$. However, with the observational uncertainties being as large as they are, it seems clear that the range of ϵ-values that are consistent with the observations is not well constrained and may be as large as 0.85 or as small as 0.5.

To show how the average apparent angular widths vary with Λ_a, we set $\Lambda_a = 1.2$ and obtained the results shown in Figure 5. Comparing Figure 5 ($\Lambda_a = 1.2$) to Figure 4 ($\Lambda_a = 1.1$), we see
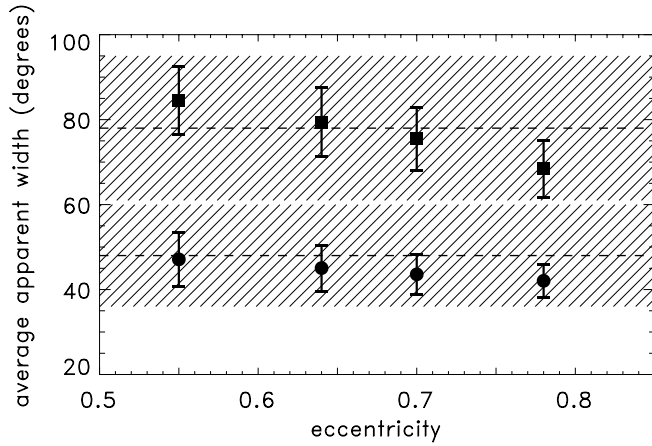
Fig. 5.—Numerically determined average angular widths for the axial (*filled circles*) and broadside (*filled squares*) cases are plotted vs. eccentricity ϵ at a fixed value of the axial aspect ratio $\Lambda_a = 1.2$. Observational results from St. Cyr et al. (2004) for the axial and broadside cases are indicated by horizontal lines at $48°$ and $78°$, respectively. Uncertainties in the observational results are indicated by shaded areas.

Fig. 6.—Synthetic coronagraph image of a "halo CME," with $\epsilon = 0.70$ and $\Lambda_a = 1.1$.

that both the average axial and average broadside widths for our parameterized flux ropes are sensitive to the axial aspect ratio Λ_a. In the case of the eccentricity ϵ, however, axial widths are notably less sensitive than broadside widths. We also see that with the large uncertainties in the observational results a deviation of 0.1 from our best-fit value of $\Lambda_a = 1.1$ produces results well within the observational uncertainty for most values of ϵ. Nevertheless, it is clear that $\Lambda_a = 1.2$ is not optimum, as that value of Λ_a provides a best fit to the observed axial angular extent with $\epsilon = 0.55$ and a best fit to the observed broadside angular extent with $\epsilon = 0.65$.

Based on these results, we conclude that the best-fit flux-rope parameters are $\epsilon = 0.7 \pm 0.2$ and $\Lambda_a = 1.1 \pm 0.3$. Note that Figures 2 and 3 feature these best-fit values: $\epsilon = 0.7$ and $\Lambda_a = 1.1$.

5. GEOMETRICAL INTERPRETATION

From the observational analysis of St. Cyr et al. (2004), which determined average apparent angular widths of $48° \pm 12°$ for the axial events and $78° \pm 17°$ for the broadside events, one might expect that a typical flux-rope CME geometry has a ratio of broadside width to axial width of $78°/48° = 1.6$. In a study that is similar to that of St. Cyr et al. (2004), Cremades & Bothmer (2005) found a roughly equivalent ratio that was also 1.6 (Cremades & Bothmer [2005] measured angular widths of specific features rather than overall angular widths). In apparent contrast to these studies, the best-fit geometry shown in Figures 2 and 3 has a ratio of broadside width to axial width of $77°/41° = 1.9$.

We find that the underlying geometry is narrower than one might expect from the observations because projection effects differ for the axial versus the broadside events. For example, consider a flux-rope CME that is viewed on the limb with the flux-rope ellipse lying in the plane of the ecliptic: this would be an exactly axial view, as shown in Figure 2a. In this case, if the source location were shifted away from the limb, the CME image would have a larger apparent angular width. Similarly, if the flux-rope ellipse were tilted out of the plane of the ecliptic, the CME image would also have a larger apparent angular width. Thus, the exactly axial angular width is thinner than the observed average apparent angular width for the axial cases.

By contrast, a flux-rope CME with an exactly broadside orientation (source at the limb and flux-rope ellipse in the plane of the
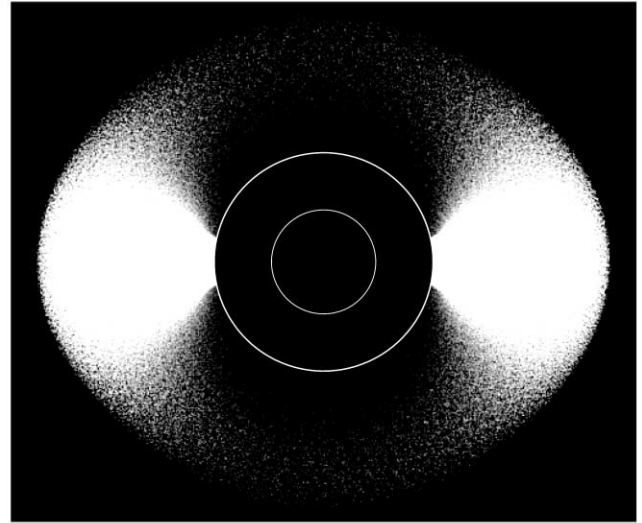
sky as in Fig. 2b) will have a smaller apparent angular width if it is tilted out of the plane of the sky. However, as in the axial configuration, shifting the source location away from the limb results in a larger apparent angular width. Our results show that these two projection effects tend to cancel for the broadside cases, with the result that the best-fit geometry has an exactly broadside angular width $77°$, a value that is close to the observed average apparent angular width of $78°$.

Our finding that the typical flux-rope CME geometry features an axial angular width of $41°$ and a broadside angular width of $77°$ raises the following question: how can a geometry with an angular width ratio of 1.9 explain a typical halo CME, with its nearly round 2D morphology? The answer lies in Figure 2, where the image in Figure 2a has a vertical width of 2.9 $R_\odot$, and the image in Figure 2b has a vertical width of 3.3 $R_\odot$. For this geometry, the resulting earth-directed halo-CME image would be nearly round ($3.3/2.9 \simeq 1.1$). This is illustrated in Figure 6, which shows a synthetic coronagraph image of a halo CME ($\alpha_y = \lambda_0 = \phi_0 = 0$), with $\epsilon = 0.7$ and $\Lambda_a = 1.1$.

Note that the synthetic halo CME image of Figure 6 shows a pair of bright circular features corresponding to the "legs" of the flux rope. Similar features are often seen in halo-CME images (see, e.g., Fig. 2 of Li et al. [2001], Fig. 5 of Manoharan et al. [2001], Figs. 3 and 8 of Yurchyshyn et al. [2001], and Fig. 1 of Krall et al. [2006]), but they are not as bright or as symmetric in our synthetic image. This is likely a weakness in our flux-rope specification, which features an approximately constant mass per unit length along the length of the flux rope; in an actual flux-rope CME, it is possible that some of this mass flows out of the legs under the force of gravity (Wang & Sheeley 2002). Also, these results are generally consistent with recent modeling of the much-studied 2003 October 28 halo-CME event (see, e.g., Gopalswamy et al. 2005 and references therein) for which Krall et al. (2006) obtained good agreement between observed and computed CME dynamics. In that case, the model CME featured $\epsilon = 0.78$ and a dynamically varying axial aspect ratio, with a typical value being $\Lambda_a \simeq 1.3$ within the LASCO field of view.

Finally, we remind the reader that the SECCHI instrument suite on the upcoming *STEREO* mission is designed to produce simultaneous coronagraph images from two viewpoints,

widely separated in space (Howard et al. 2000). Using these data, it should be possible to determine the underlying geometry for individual CME events, providing a good test of our results.

APPENDIX

SYNTHETIC CORONAGRAPH IMAGES

For the purpose of constructing the synthetic coronagraph images of Figures 2, 3, and 6, we have developed a numerical method of generating a three-dimensional (3D) representation of the flux-rope CME density, based on the parameters of the flux-rope ellipse, eccentricity ϵ and major-axis length $2R_1$, and the width of the flux rope at the apex, d (see Fig. 2).

We define the inner and outer edges of the flux rope, which lie in the same plane as the flux-rope axis, to be ellipses with eccentricities ϵ and major-axis lengths $2R_1 \pm d/2$. These inner and outer ellipses are arranged such that the width of the flux rope is d at the apex and 0 at the "footpoints," where this idealized flux rope contacts the solar surface. Thus, the local flux-rope width varies from $d(\phi) = 0$ to $d(\phi) = d$ as indicated in Figure 7. Finally, for each value of ϕ we assume that the cross-section of the flux rope is circular with radius $d(\phi)/2$.

For the purpose of computing synthetic coronagraph images, we specify the density of free electrons n_e at each point in space, and compute the Thomson scattering of light as in Billings (1966). For simplicity, we assume that the density per unit length is constant versus ϕ, and that the density at fixed ϕ is a function only of the distance r from the flux-rope axis. We therefore need only specify the function $n_e(r/d)$ to complete our description of the flux rope. In so doing, however, we neglect any prominence material that might be present.

Assuming that a flux-rope CME results from the eruption of a coronal flux rope, we can use one of the density profiles from Krall & Chen (2005) for our function $n_e(r/d)$. This application of the pre-eruption density structure to the posteruption CME is supported by model calculations (Krall et al. 2000), which show that a typical erupting flux rope accelerates rapidly beyond the point where the CME apex velocity exceeds the sound speed within the flux rope. That is, typical subsonic flows are too slow to affect the density structure near the apex during the eruption. In all cases, we used the density profile shown in Figure 5 of Krall & Chen (2005) with the argument r/a of Krall & Chen (2005) replaced here with $2r/d$. Note that our methodology is generally similar to that of Chen et al. (2000) where an ad hoc density profile was specified in order to produce model synthetic coronagraph images corresponding to a specific CME event and where the flux rope was assumed to be circular rather than elliptical.

In producing synthetic coronagraph images for comparison to LASCO images, one must account for the effect of background subtraction, in which an average observed coronal brightness is subtracted from each image, and the effect of vignetting. Each of these effects tends to dim the inner portion of the image relative to the outer portion. It has been estimated that, for the LASCO/C2 and C3 coronagraphs, these effects can be accounted for by multiplying the computed brightness by a factor of R_i^n where R_i is the heliocentric distance within the image plane and $2 \leq n \leq 3$ (Chen et al. 2000). In our images, we have used $n = 2.5$.

Finally, we note that our synthetic coronagraph images are generated by arraying a large number of "particles" over the volume of the flux rope, assigning a weight to each particle, and allowing each particle to contribute to the computed image. In this way, the orientation of the flux rope, described in § 3, is accomplished via rotations and translations of these particles (of course the Thomson scattering is computed after the particles are rotated to their final positions). These "particles," which are employed to keep these rotations and translations as simple as possible, give the images a somewhat grainy appearance.
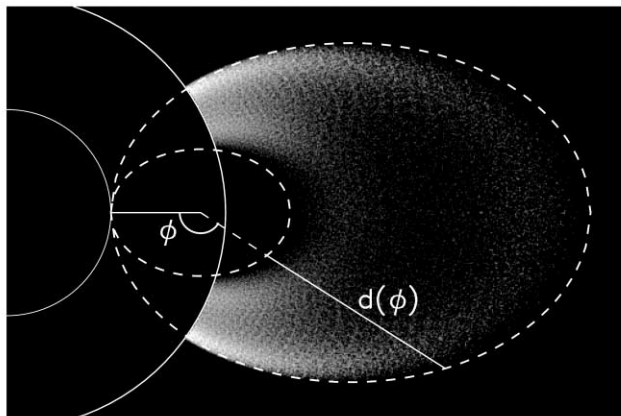

Fig. 7.—Synthetic coronagraph images of a parameterized flux rope showing axial view as in Fig. 2. Local width $d(\phi)$ is indicated.

REFERENCES

Billings, D. E. 1966, A Guide to the Solar Corona (New York: Academic Press)
Brueckner, G. E., et al. 1995, Sol. Phys., 162, 357
Chen, J., & Krall, J. 2003, J. Geophys. Res., 108, SSH 2-1
Chen, J., et al. 1997, ApJ, 490, L191
———. 2000, ApJ, 533, 481
Cremades, H., & Bothmer, V. 2004, A&A, 422, 307
———. 2005, in IAU Symp. 226, Coronal and Stellar Mass Ejections, ed. K. Dere, J. Wang, & Y. Yan (Cambridge: Cambridge Univ. Press), 48
Dere, K. P., Brueckner, G. E., Howard, R. A., Michels, D. J., & Delaboudinière, J. P. 1999, ApJ, 516, 465
Fisher, R. R., & Munro, R. H. 1984, ApJ, 280, 428
Gopalswamy, N., Barbieri, L., Lu, G., Plunkett, S. P., & Skoug, R. M. 2005, Geophys. Res. Lett., 32, L03S01
Howard, R. A., Michels, D. J., Sheeley, N. R., Jr., & Koomen, M. J. 1982, ApJ, 263, L101
Howard, R. A., Moses, J. D., & Socker, D. G. 2000, Proc. SPIE, 4139, 259
Howard, R. A., Sheeley, N. R., Jr., Koomen, M. J., & Michels, D. J. 1985, J. Geophys. Res., 90, 8173
Hundhausen, A. 1999, in The Many Faces of the Sun, ed. K. T. Strong, et al. (New York: Springer), 143
Illing, R. M. E., & Hundhausen, A. J. 1986, J. Geophys. Res., 91, 10951
Krall, J., & Chen, J. 2005, ApJ, 628, 1046
Krall, J., Chen, J., Duffin, R. T., Howard, R. A., & Thompson, B. J. 2001, ApJ, 562, 1045

Krall, J., Chen, J., & Santoro, R. 2000, ApJ, 539, 964
Krall, J., Yurchyshyn, V. B., Slinker, S., Skoug, R. M., & Chen, J. 2006, ApJ, 642, 541
Li, Y., Luhmann, J. G., Mulligan, T., Hoeksema, J. T., Arge, C. N., Plunkett, S. P., & St. Cyr, O. C. 2001, J. Geophys. Res., 106, 25103
Manoharan, P. K., et al. 2001, ApJ, 559, 1180
Plunkett, S. P., et al. 2000, Sol. Phys., 194, 371
Reif, F. 1965, in Fundamentals of Statistical and Thermal Physics (New York: McGraw-Hill), 584
St. Cyr, O. C., Cremades, H., Bothmer, V., Krall, J., & Burkepile, J. T. 2004, in American Geophysical Union, Fall Meeting 2004 (San Francisco: AGU), abstract SH22A-04
Wang, G., & Sheeley, N. R., Jr. 2002, ApJ, 567, 1211
Webb, D. F., Cliver, E. W., Crooker, N. U., St. Cyr, O. C., & Thompson, B. J. 2000, J. Geophys. Res., 105, 7491
Wood, B. E., Karovska, M., Chen, J., Brueckner, G. E., Cook, J. W., & Howard, R. A. 1999, ApJ, 512, 484
Wu, S. T., Guo, W. P., Michels, D. J., & Burlaga, L. F. 1999, J. Geophys. Res., 104, 14789
Yurchyshyn, V. B., Liu, C., Abramenko, V., & Krall, J. 2006, Sol. Phys., in press
Yurchyshyn, V. B., Wang, H., Goode, P. R., & Deng, Y. 2001, ApJ, 563, 381